

MATHEMATICAL MODELING OF FIRE-INDUCED FLASHOVER DUE TO DEPOSITION OF SOOT PARTICLES ON SUSPENSION INSULATORS OF A HVTL

Emad H. El-Zohri^{a,*}, M. Abdel-Salam^b, Hamdy M. Shafey^c, and A. Ahmed^b

^a *Electrical Engineering Department, Faculty of Industrial Education, Sohag University, Sohag, Egypt*

^b *Electrical Engineering Department, Faculty of Engineering, Assiut University, Assiut, Egypt*

^c *Mechanical Engineering Department, Faculty of Engineering, Assiut University, Assiut, Egypt*

(Received November 27, 2011 Accepted Jaunayr1 5, 2012)

This paper presents a mathematical integrated model that simulates the coupled events causing flashover due to the deposition of soot particles on suspension insulators of high voltage transmission lines (HVTL). The model considers non-steady three-dimensional multi-phase flow of agricultural fire producing the soot particles. In addition, the model describes in detail the mechanism of the soot deposition combined with the developing of the electric field. The model equations are simultaneously solved using an iterative finite-volume numerical technique together with the indirect boundary element and charge simulation methods. The model validity and accuracy are verified through the discussion of the results for a representative case study of a 15 kV cap-and-pin insulator string. The discussion includes a comparison of the present numerical predictions for characteristics of the deposited soot layer, electric field distribution, and characteristics of flashover occurrence, with the available results in the literature.

KEYWORDS: *Mathematical model, Agricultural fires modeling, Soot deposition, and Fire-induced flashover*

1. INTRODUCTION

High voltage transmission lines (HVTL) usually cross agricultural fields in which accidental fires may occur. Also, farmers intentionally burn crop residues in such agricultural fields as a harvesting aid. The occurring agricultural fires result in environmental impact represented by thermal and gaseous pollution accompanied with the production of soot particles. The soot particles deposited on the insulator surface of the high voltage transmission lines are often reported to cause flashover and consequently, the outages of these lines. In some tropical countries, the number of line outages due to fires, whether intentional or accidental, can be up to hundreds a year per line [1]. This leads to a great economic loss for both the utility and users.

* Corresponding author: Tel.: +20-88-2299037; Fax: +20-88-332553
E-mail address: emad.elzohri@yahoo.com

NOMENCLATURE

D_ϕ	The effective diffusion coefficient of any transported variable ϕ	x_j	x, y, z Cartesian coordinates in tensor notation
E	Magnitude of electric field strength, $V.m^{-1}$	<i>Greek symbols</i>	
g_i	Gravity vector, $m.s^{-2}$	δ_{SL}	Soot layer thickness, m
I	Current, A	ψ	Surface charge density, $C.m^{-2}$
m_p^{acc}	Mass of accumulated soot particles, kg	ϕ	Any transported variable
Q_i	Discrete charges, C	ρ_p	Density of the soot particles
R	Resistance, Ω	σ_{SL}	Electric conductivity of soot layer, $S.m^{-1}$
t	Time, s	τ	Time constant
T	Temperature of the gas mixture, K	θ	Incident angle of soot particles
T_{SL}	Temperature of soot layer, K	<i>Subscripts and superscripts</i>	
u_i	Velocity vector of gas phase, $m.s^{-1}$	n	Normal component
u_{p_i}	Velocity vector of soot particles, $m.s^{-1}$	p	Soot particles
V_p	Electric potential at any point p, V	t	Tangential component

Accurate modeling of the flashover mechanism requires deep understanding and appropriate formulation of the equations governing the physical and chemical processes associated with combustion, spread of fire, and deposition of fire-produced soot particles. The presence of electric field of the energized transmission line affects the flow and deposition of soot particles as the solid phase of the multi-phase flow of the fire products. The deposited soot layer results in an increasing leakage current over the insulator surface which by turn leads to the flashover of high voltage insulators. Most of the published works [2 – 6] on mathematical modeling of combustion and fire spread were generally limited due to simplifying assumptions which can not be extended to many of the real cases. Recently, the present authors developed a more realistic mathematical three-dimensional non-steady fire model [7] as a preparatory stage of the present work.

The research works on topics related to fire spread investigate models and measurements of turbulent gas-particle flow and the soot particles deposition [8 – 10]. Current approaches commonly used to simulate turbulent gas-particle flow in computational fluid dynamics (CFD) are the Eulerian-Eulerian and the Eulerian-Lagrangian models [11,12]. In the Eulerian-Eulerian approach, both the gas and particle flows are treated as continuous fluid flow and regarded as interacting with each other. In the Eulerian-Lagrangian approach, the Eulerian equations of the gas phase are

solved and the Lagrangian equations of particle motion are integrated by tracking individual particle through the flow field. Tian [13] investigated the performance of the two gas-particle models, and developed particle-wall collision models describing the associated boundary conditions. Zhang & Chen [14] used a modified Lagrangian method to predict particle deposition onto indoor surfaces. Valentine & Smith [15] described a model coupled with a particle cloud tracking technique for predicting particle deposition in turbulent flow fields. Cohan [16] experimentally validated a more specific model for the soot deposition in fire dynamics simulator (FDS). Important factors in soot deposition modeling are the particle deposition velocity and soot material properties. These factors can be determined using measurements, models, and properties in different published works [8,17,18].

Numerous works have been devoted to understand the phenomena leading to flashover of polluted insulators in order to elaborate a model allowing one to predict accurately the critical flashover voltage. A common limitation for most proposed models [19 – 23] is the simplified static representation of propagating arc in series with the resistance of the polluted layer. Proposed models in the last three decades individually considered various parameters such as arc dynamics [24 – 28], the chemical nature of the pollutants [29], and multiple arcs [30]. The discussed published works are valuable as a first simple approach for the separate topics (fire model, soot deposition, and flashover mechanism) involved in the real complex case of fire-induced flashover.

The aim of the present work is to formulate and solve a non-steady three-dimensional mathematical integrated model for the flashover mechanism due to the deposition of fire-produced soot particles on high voltage insulators. This model accurately simulates the coupled real events of the multi-phase flow produced by agricultural fires occurring beneath a high voltage transmission line. Also, the model introduces a detailed treatment of soot particles deposition on the insulator string units with a precisely described geometry. The features of this geometry are key factors in flow and deposition of soot particles, electric field distribution, and consequently, flashover criterion. The model equations are simultaneously solved using an iterative finite-volume numerical technique together with charge simulation and indirect boundary element methods for calculating the electric field distribution. Model numerical predictions are presented and discussed for a representative case study to check the model validity and accuracy. These predictions include characteristics of the deposited soot layer, electric field distribution, and characteristics of flashover occurrence.

2. MATHEMATICAL FORMULATION

The present mathematical model analyzes the transport phenomena including fire products leading to the flashover, specifies the conditions for the agricultural fire model, and describes the transmission line insulator boundary and the associated processes occurring at this boundary. The model includes the basic system of differential and integral equations that govern the transport phenomena, with corresponding initial and boundary conditions. The model equations are simultaneously solved using an iterative finite-volume numerical technique. The following sub-sections describe the details of the present mathematical model.

2.1 Theoretical Model and Basic Assumptions

Figure 1 shows the important features describing the theoretical model including the agricultural fire model and the insulator string model. The figure shows the coordinate system, dimensions, and the associated outer boundaries of the computational domain. A wind-driven fire propagates in x -direction through the agricultural fuel bed of a depth δ_M , width W_M , and length L_M forming a flame with a height H_M . The associated dimensions L_C , W_C , and H_C of the computational domain are expressed in terms of those for the conceptual structure representing the agricultural fire model. These selected dimensions are large enough to agree with the practical considerations of computational fluid dynamics (CFD) for wind environment around structures [31]. The insulator string consisting of N identical rotationally-symmetric units is stressed by a system voltage V_{system} at a height H_{st} with respect to the ground plane. The vertical axis of the insulator string is located in the symmetry plane of the computational domain, at a horizontal length L_{st} from the fire model. Usually, the height H_M of the occurring fire beneath the transmission line is less than the height H_{st} with a distance enough to assume that the effect of the electric field can be neglected in the space down to H_M . The conditions of the fire model generally produce identical spatial variations of the flow properties around the symmetry plane of the computational domain. This suggests that only half of the computational domain is sufficient to describe precisely the flow with less computation. Moreover, half of the computational domain can be divided into two distinct spaces. The flow in the lower space down to the flame height H_M is treated as a multi-phase medium with fire model equations and associated initial and boundary conditions are previously formulated and presented [7]. On the other hand, the upper space above the flame height H_M is concerned with the multi-phase flow of the fire products with carrier gas phase is the combustion gases. The associated solid phase is the dispersed soot particles which are affected by the electric field. The following basic assumptions are considered in the present mathematical formulation.

- (1) The flow of the solid phase representing the soot particles, is treated only with the continuity and momentum equations.
- (2) The soot particles are considered in thermal equilibrium with the gas phase.
- (3) The diffusion and the turbulence terms in the momentum equations for the solid phase are neglected.
- (4) No chemical reactions are considered in the flow equations.
- (5) The effects of any objects (e.g. buildings, towers, trees ...), existing within the computational domain, are neglected and attention is focused only on the insulator string.

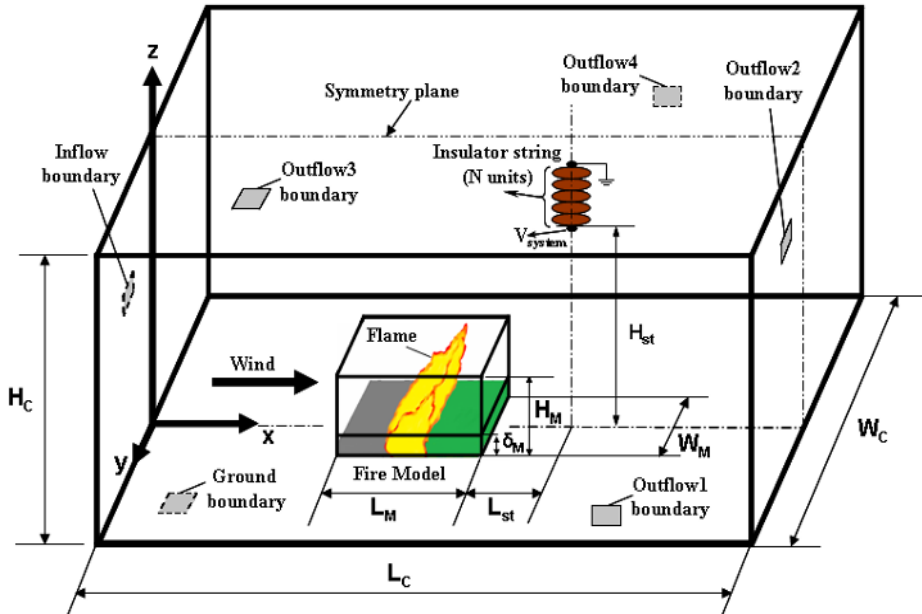


Fig. 1 General features of the theoretical model and the computational domain

2.2 Modeling the Multi-phase Flow of the Fire Products

2.2.1 Basic Equations for the Carrier Gas Phase

The general form of the balance equations for the gas phase flow can be expressed by the following elliptic partial differential equation [4-6]:

$$\frac{\partial (\rho \phi)}{\partial t} + \frac{\partial (\rho u_j \phi)}{\partial x_j} = \frac{\partial}{\partial x_j} \left(D_\phi \frac{\partial \phi}{\partial x_j} \right) + S_\phi, \quad (1)$$

where ϕ is the generic form of the transport fluid property having a corresponding diffusive exchange coefficient D_ϕ and a source term S_ϕ . Expressions for D_ϕ and S_ϕ are reported for the fire model [7]. Modified expressions for S_ϕ are formulated to consider the conditions of the present model.

2.2.2 Solid Phase

The dispersed mono-sized soot particles representing the solid phase can be treated as a quasi-fluid continuum [13] of a density ρ_p , flowing with velocity components u_{p_i} . The flow behaviour of this solid phase is controlled by the following continuity and momentum equations, in tensor notation.

$$\frac{\partial \rho_p}{\partial t} + \frac{\partial (\rho_p u_{p_j})}{\partial x_j} = 0, \quad (2)$$

$$\frac{\partial (\rho_p u_{p_i})}{\partial t} + \frac{\partial (\rho_p u_{p_j} u_{p_i})}{\partial x_j} = \rho_p g_i + \tau \rho_p (u_i - u_{p_i}) + \varepsilon_0 \frac{\partial E^2}{\partial x_i}, \quad (3)$$

where τ is a time constant, u_i are the velocity components of the gas phase, ε_0 is the dielectric constant of air, and E is the magnitude of electric field strength. The R.H.S. of Eq. (3) consists of three source terms representing the gravitational force, the drag force (momentum exchange), and the electrophoretic force.

2.2.3 Initial and Outer Boundary Conditions

The initial conditions represent the values of the flow properties for both gas and solid phases, just at the beginning instant of the fire (at $t = 0$) when the flow properties are those for the free stream (clean soot-free atmospheric air) [7]. Referring to Fig.1, the outer boundary conditions for the flow of the fire products can be described as follows. The conditions at the planes $x = 0$ and $x = L_C$ are inflow and outflow, respectively. The conditions at the planes $y = 0$ and $y = W_C/2$ are symmetry and outflow, respectively. The condition at the plane $z = H_C$ is outflow. The condition at the interface plane $z = H_M$ is formulated by the continuity of the flow properties for both multi-phase flows down (fire model) and above this plane.

2.3 Modeling of the Inner Boundary Conditions and Soot Deposition on the Insulator Surface

This sub-section is devoted for satisfactory modeling of the geometry of the insulator surface representing the inner boundary and the corresponding flow conditions. In addition, various processes occurring at this boundary are analyzed to estimate the thickness and temperature of the deposited soot layer polluting the insulator.

2.3.1 Description of the Insulator Geometry

The insulator string consists of N identical units connected to each other as shown in Fig. 1. Consequently, a representative geometric description of the surface for one unit is demonstrated. Figure 2 shows the main features of the geometry for the unit model. The unit can be approximated by an oblate spheroid (Fig. 2a). The spheroid is located at a center O' (x_u, y_u, z_u) as shown in Fig. 2b. The spheroid surface is obtained by rotating the half of an ellipse about its minor axis (z'). The angle of rotation λ (0 to 2π) and the angle of ellipse generation β ($-\pi/2$ to $\pi/2$) are the surface description parameters (Fig. 2b). The half-lengths a and b of the major and minor axes, respectively, are obtained from the real dimensions of the insulator unit. The tangent plane at a point P and the corresponding outward normal vector are necessary for the formulation of the boundary conditions at the unit surface. The description of these items in terms of the surface parameters λ and β is mathematically straightforward.

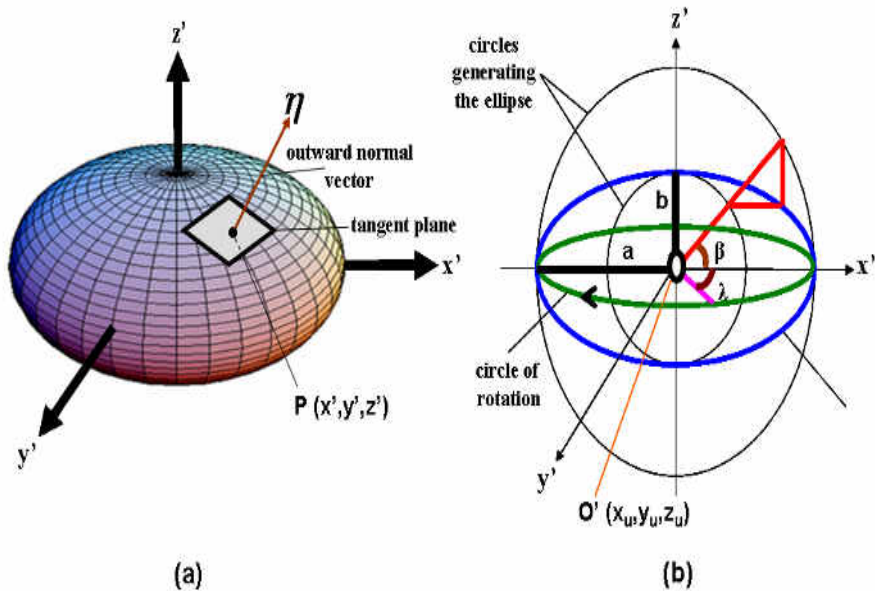


Fig. 2 Main features of the geometric model for the insulator unit:
 (a) The spheroid surface of the model, (b) Surface parameters and dimensions.

2.3.2 Boundary Conditions for the Gas Phase

Considering the gas flow, the insulator represents a boundary of curved solid non-porous wall. At this boundary, the no-slip condition for the velocity components and turbulence applies. An appropriate thermal condition at the insulator surface is that the value of the gas temperature equals the value of the soot layer temperature which is determined later. The impermeability condition is applied for the mass fractions of the gas phase species.

2.3.3 Boundary Conditions for the Solid Phase

The conditions of the solid phase particles at the insulator surface can be identified through inter-relations for the particles velocity vector and density. The application of this concept deals with the choice of a control space adjacent to the specified point P on the insulator surface. Figure 3 shows such a control space which is bounded by the tangent plane at the point P and an imaginary parallel plane at a height h (much larger than the thickness of the deposited soot layer). The soot particles arriving at the insulator surface with incident velocity vector V_w and density $\rho_{p,w}$ suffer rebounding with restitution coefficients associated with the inward normal component $u_{n,w}^P$ and the tangential component $u_{t,w}^P$. Both incident and reflected velocities constitute the flow velocity field in the control space adjacent to the point P. Also, mass of the soot particles is conserved for this control space.

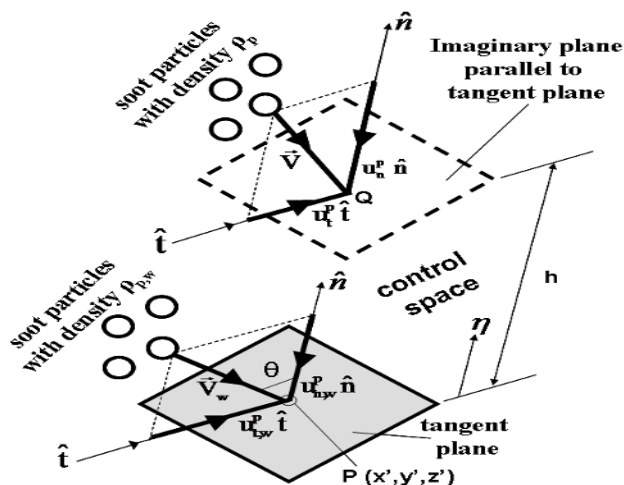


Fig. 3 The control space with the soot particle velocity vector components.

Neglecting the effect of soot deposition on mass conservation, the boundary conditions can be identified by the following generic equation [13].

$$a \phi_w + b \left. \frac{\partial \phi}{\partial \eta} \right|_w = c \quad , \quad \phi = [u_n^p, u_t^p, \rho_p] \quad (4)$$

The associated coefficients a , b , and c are expressed in terms of restitution coefficients e_n and e_t . These are functions of the incident angle $\theta = \tan^{-1}(u_{t,w}^p / u_{n,w}^p)$ [13], and are given by

$$e_n = 0.993 - 1.76\theta + 1.56\theta^2 - 0.49\theta^3 \quad (5)$$

$$\text{and } e_t = 0.988 - 1.66\theta + 2.11\theta^2 - 0.67\theta^3. \quad (6)$$

The inward normal velocity incident at the insulator surface $u_{n,w}^p$ must exceed a value known as capture velocity, u_c for the soot particles to rebound from the insulator surface. So, for $u_{n,w}^p \leq u_c$ both of the restitution coefficients e_n and e_t are equal to zero. The capture velocity u_c depends on many factors (e.g. particle size and material, insulator surface conditions ...), and is to be determined experimentally. Based on the available data in the literature, a reasonable value of $u_c = 0.001$ m/s for soot particles is adopted [8 – 10]. The differential form of the generic equation (Eq. (4)) is transformed to a linear algebraic equation in the unknown ϕ_w . This is achieved

by substituting for the derivative $\left. \frac{\partial \phi}{\partial \eta} \right|_w$ with its forward numerical formula in terms of the value of ϕ at $\eta = h$. A two-way transformation between the velocity components

u_n^p and u_t^p , and their corresponding Cartesian components u_{p_i} for the coupling of the generic equation with the flow momentum equation (Eq. (3)).

2.3.4 Soot Layer Thickness

The soot particles with normal velocities $u_{n,w}^p$ less than or equal to the capture velocity u_c are liable to deposit on the insulator surface. Therefore, the local instantaneous deposition flux of soot particles $(DF)_p$ can be estimated by

$$(DF)_p = \rho_{p,w} u_{n,w}^p, \quad u_{n,w}^p \leq u_c \tag{7}$$

The local instantaneous accumulated mass of deposited soot particles per unit area m_p^{acc} is calculated as

$$m_p^{acc} = \int_0^t (DF)_p dt \tag{8}$$

The local instantaneous soot layer thickness δ_{SL} on the insulator surface is estimated as

$$\delta_{SL} = \frac{m_p^{acc}}{\rho_{SL}}, \tag{9}$$

where the soot-layer density $\rho_{SL} = (1 - \varepsilon_v)\rho_{soot}$. The voidage ratio ε_v for loose packing of soot particles can be taken as 0.45 and the bulk density of the soot material ρ_{soot} is taken to be 1800 kg/m³ [5].

2.3.5 Soot Layer Temperature

The local instantaneous temperature of the soot layer is controlled by different thermal energy processes. They are classified as thermal energy generation due to the flow of a leakage current, two-dimensional heat conduction, and heat convection to the surrounding gas phase. Neglecting the heat conduction to the insulator bulk material and performing an energy balance, one can obtain the two-dimensional non-steady differential equation for the soot layer temperature T_{SL} as

$$\frac{\partial T_{SL}}{\partial t} = D_{SL} \left[\frac{1}{\delta_{SL}} \frac{\partial}{\partial L} \left(\delta_{SL} \frac{\partial T_{SL}}{\partial L} \right) + \frac{1}{\delta_{SL}} \frac{\partial}{\partial S} \left(\delta_{SL} \frac{\partial T_{SL}}{\partial S} \right) + \frac{\sigma_{SL} E_{i,L}^2}{K_{SL}} + \frac{K_{gas}}{\delta_{SL} K_{SL}} \frac{\partial T}{\partial \eta} \Big|_w \right], \tag{10}$$

where L is the leakage path length and S is the length on a circle of rotation.

The properties D_{SL} and K_{SL} are the thermal diffusivity and conductivity of the soot layer, respectively, while K_{gas} is the thermal conductivity of the gas phase. The

convective heat is expressed in terms of the gas temperature gradient $\frac{\partial T}{\partial \eta} \Big|_w$ in the outward normal direction at the insulator surface. The thermal energy generation term

includes the tangential component of the electric field strength $E_{t,L}$ along the leakage path length. The term also includes the temperature-dependent electric conductivity σ_{SL} of the soot layer, which is an important factor in determining the electric field affecting the soot deposition process. Equation (10) can be solved numerically using appropriate initial and boundary conditions.

2.4 Electric Field Distribution

The presence of the deposited soot layer polluting the insulator surface distorts the capacitive potential distribution and the electric field is no longer capacitive but may be capacitive-resistive or resistive, depending on the severity of the surface pollution. The algorithm developed for calculating the electric capacitive-resistive field distribution is based on the indirect Boundary Element Method and the Charge Simulation Method. The insulator under investigation (Fig. 2) is surrounded by air and is stressed between a pair of electrodes (cap and pin). The top electrode is taken as grounded while the bottom electrode is stressed by the applied voltage. Since the insulator-electrodes assembly is a rotationally-symmetric configuration, ring charges [33] are employed for simulation. Each electrode is simulated by a set of N_e ring charges placed within the electrode. The insulator-air interface is simulated by two sets of $2N_d$ ring charges, one set placed in insulator and other set in air. Images of the fictitious ring charges with respect to the ground plane are also considered in the present algorithm. For power frequency capacitive-resistive field calculation, complex fictitious charges varying sinusoidally with time are employed to give the instantaneous field distribution [34,35]. The electrodes and insulator boundaries are discretized into several boundary elements and a suitable polynomial is introduced for the equivalent surface charges along the discrete boundary elements. Then the electric field in the region of interest is considered to be caused by the equivalent surface charges along the boundary elements. The potential $\Delta V_{p,d}$ at a space point p with ordinate r' due to the surface charges within a finite element of area ΔA (Fig. 4) is expressed by the Fredholm integral equation of the first kind as

$$\Delta V_{p,d} = \frac{1}{4\pi\epsilon} \int_{\Delta A} \frac{\psi(\beta, \lambda)}{|r' - r|} dA \quad , \quad (11)$$

where dA is the differential area centered at a surface point $P(\beta, \lambda)$ with space ordinate r , $\psi(\beta, \lambda)$ is the corresponding surface charge density, and ϵ is the dielectric constant. The surface charge density $\psi(\beta, \lambda)$ can be expressed as a simple 4terms-polynomial [36]. Substituting for $\psi(\beta, \lambda)$, r' , and dA in terms of β and λ , Eq. (11) can be re-written as

$$\Delta V_{p,d} = \frac{1}{4\pi\epsilon} \int_{\beta_1}^{\beta_2} \int_{\lambda_1}^{\lambda_2} \frac{(k_0 + k_1 \beta + k_2 \lambda + k_3 \beta \lambda) (a \cos \beta \sqrt{a^2 \sin^2 \beta + b^2 \cos^2 \beta} d\beta d\lambda)}{\sqrt{(x_u + a \cos \beta \cos \lambda - x)^2 + (y_u + a \cos \beta \sin \lambda - y)^2 + (z_u + b \sin \beta - z)^2}} \quad (12)$$

The four coefficients of this polynomial (k_0 , k_1 , k_2 , and k_3) can be given in terms of the coordinates (β_1 , β_2 , λ_1 , and λ_2) and the charge densities (ψ_1 , ψ_2 , ψ_3 , and ψ_4) of the four vertices of the element ΔA (Fig.4). Integrating and surveying all elements of the insulator string, one can get the potential $V_{p,d}$ at the point p due to all surface charge densities as a summation over $2N_d$ unknown surface charge densities ψ_i , $i = 1, 2, \dots, 2N_d$ each multiplied by a corresponding potential coefficient function. A similar summation can be considered for the contribution of the potential $V_{p,e}$ at the point p due to $2N_e$ unknown discrete charges Q_i , $i = 1, 2, \dots, 2N_e$ simulating the electrodes. Thus the total potential V_p can be expressed as

$$V_p = V_{p,e} + V_{p,d} = \sum_{i=1}^{2N_e} P_{e,i} \cdot Q_i + \sum_{i=1}^{2N_d} P_{d,i} \cdot \psi_i \quad (13)$$

where $P_{e,i}$ and $P_{d,i}$ are the potential coefficient functions due to discrete charges simulating the electrodes and due to surface charge densities on the insulator surface, respectively.

The electric field strength at the point p can be obtained as $E_p = -\nabla V_p$, and the tangential component along the leakage path is given by $E_{t,L} = \frac{\partial V_p}{\partial L}$.

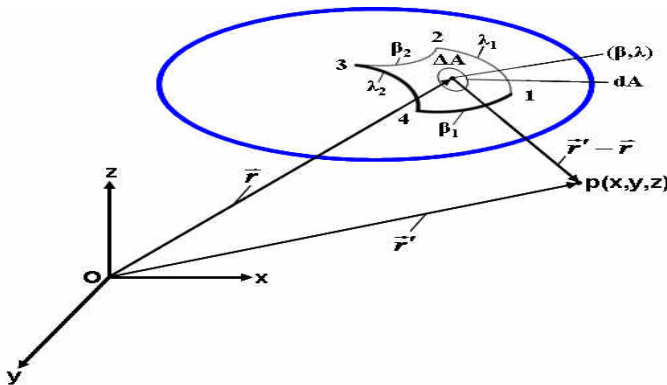


Fig. 4 Spheroidal element.

The unknown discrete charges Q_i and surface charge densities ψ_i in Eq. (13) are chosen such that they satisfy the following boundary conditions.

Dirichlet's condition on the electrode surface is

$$V_p = V_e \quad (14)$$

where V_e is the known potential on the HV electrode and the grounded electrode with respective values of system voltage V_{system} and zero.

Potential continuity condition on the insulator-air interface (insulator surface) is

$$V_p \Big|_{\varepsilon=\varepsilon_{insulator}} = V_p \Big|_{\varepsilon=\varepsilon_0} \quad , \quad (15)$$

Continuity condition of the normal component of the electric flux density D_n on the insulator surface is

$$D_n \Big|_{\varepsilon=\varepsilon_{insulator}} - D_n \Big|_{\varepsilon=\varepsilon_0} = \psi_{true} \quad , \quad (16)$$

where ψ_{true} is the true surface charge density. The numerical value of the true surface charge density $\psi_{true,ij}$ at a surface point p , node i, j , is calculated in terms of the potentials at the specified node and the surrounding nodes as

$$\psi_{true,ij} = \frac{1}{i\omega} \frac{1}{\Delta A_{ij}} \left[\frac{(V_p)_{i-1,j} - (V_p)_{i,j}}{R_i} - \frac{(V_p)_{i,j} - (V_p)_{i+1,j}}{R_{i+1}} + \frac{(V_p)_{i,j-1} - (V_p)_{i,j}}{R_j} - \frac{(V_p)_{i,j} - (V_p)_{i,j+1}}{R_{j+1}} \right] \quad , \quad (17)$$

where $i = \sqrt{-1}$, ω is the angular frequency, and $\Delta A_{ij} = (\Delta L \cdot \Delta S)_{ij}$ is the element surface area at the node i, j .

The resistances R_i , R_{i+1} , R_j , and R_{j+1} in Eq. (17) are calculated in terms of the local surface resistance R_{SL} at the different nodes, and the associated differences of ΔL and ΔS . The local surface resistance R_{SL} is the reciprocal of the product of the local soot layer thickness δ_{SL} and conductivity σ_{SL} .

2.5 Flashover Criterion

The leakage current increases due to the accumulated deposition of the soot layer. This increase in the leakage current continues to the extent causing start of partial arcs (discharges) along the leakage path. With further increase in the leakage current, these partial arcs elongate and join to cause flashover occurrence. This requires a condition that the arc length bridges as much as 67% of the total leakage path length [37].

The start of discharge at a specified point on the insulator surface is controlled by the arc propagation criterion ($E_{t,L} > E_{arc,L}$), where the arc electric field strength along the leakage path $E_{arc,L}$ can be expressed in terms of the leakage current I_L by

$$E_{arc,L} = A I_L^{-n} \quad (18)$$

For air environment, the arc constants take the values $A = 63$ and $n = 0.76$ [28]. The leakage current I_L can be estimated as the average of its local numerical values $I(L_i)$ (passing through finite circular rings along the leakage path), calculated by

$$I(L_i) = 2 \sum_{j=1}^m \left(\sigma_{SL} E_{t,L} \delta_{SL} \Delta S \right)_{ij} \quad (19)$$

where m is the number of the j^{th} nodes over the i^{th} finite ring and $(\Delta S)_{ij}$ is the difference length on the corresponding half ring.

2.6 Numerical Solution

The differential equations of the present mathematical model are simultaneously solved using an iterative finite-volume numerical technique. The multi-phase flow equations are discretized on a staggered, nonuniform Cartesian three-dimensional grid of finite cells. A second-order backward Euler scheme is used for time integration. A second-order central difference scheme is used to approximate the diffusion terms. The resulting discretized equations are a system of linear algebraic equations which are solved iteratively using the line-by-line tridiagonal matrix algorithm [38]. In order to accelerate convergence, all the flow properties are underrelaxed using inertial relaxation. The charge simulation method and the indirect boundary element method are used for the numerical calculation of the electric field distribution. Usually, it is needed to predict numerical results for a specific case within assigned time. The running of calculations is completed unless the condition of flashover occurrence is satisfied before this time.

3. RESULTS AND DISCUSSION

The present mathematical model was simulated by a computer program which has been developed and processed to test the model validity and accuracy. A representative case study of single-phase high voltage transmission line with a single insulator string is selected to perform this task. The transmission line crosses an agricultural fuel bed of natural tall grassland in which a wind-driven fire propagates. The main input data relevant to the transmission line and the agricultural fire model are listed in Table 1. These data are the same for all numerical results predicted by the present model, except otherwise stated. Useful data of the fuel bed properties and the associated fire conditions are presented before [7]. A satisfactory numerical solution is obtained using a grid of $1044 \times 360 \times 348$ cells. The cells in the fuel bed region are sub-divided into a refined mesh of $200 \times 30 \times 80$ small cells. The cells adjacent to the insulator boundary are sub-divided into a refined mesh of $186 \times 6 \times 1$ small cells. In addition, a fine step of 0.025 s for time domain was taken to accelerate convergence. The convergence of the iterations for each cell is considered to be reached when the criterion $\left| \Phi^{n+1} - \Phi^n \right| / \left| \Phi^n \right| \leq 10^{-4}$ is satisfied for a flow property Φ . The following discussion is made on some selected model predictions which are strongly related to the soot deposition on the insulator surface and the resulting flashover characteristics.

Table 1 Main input data for the transmission line and the agricultural fire model.

Item	Value
System voltage (V_{system}), kV	15
Number of insulator string units (N)	6
Leakage path length of an insulator string unit, mm	310
Maximum diameter ($2a$) of an insulator string unit, mm	252
Height ($2b$) of an insulator string unit, mm	146
Horizontal length between insulator string and fire model (L_{st}), m	1
Height of insulator string above the ground (H_{st}), m	9
Length of fire model (L_M), m	100
Width of fire model (W_M), m	40
Height of fire model (H_M), m	8
Length of computational domain (L_C), m	261
Width of computational domain (W_C), m	120
Height of computational domain (H_C), m	48
Fuel bed depth (δ_M), m	0.8

3.1 Characteristics of the Deposited Soot Layer

Figures 5 to 8 show the results for the distribution and time evolution of the main properties (thickness, temperature, surface resistance) of the deposited soot layer as well as the effect of system voltage on the soot layer thickness. Hereafter, a property distribution is represented by the continuous variation along the whole leakage path length for representative path lengths with A: $\lambda = 180^\circ$ (front), B: $\lambda = 120^\circ$, C: $\lambda = 60^\circ$, and D: $\lambda = 0^\circ$ (rear).

Figure 5 shows the time evolution for the distribution of the deposited soot layer thickness. For all time instants, the soot layer thickness has large values at front leakage paths and then decreases towards the rear location. This is expected due to the combined effects of the insulator string geometry and the dominant velocity direction of the incident soot particles. For first instants ($t = 60$ s) after the beginning of the fire ($t = 0$), a non-uniformity of the soot layer thickness is noticeable from its variation along the leakage path length. The soot layer thickness approaches nearly constant values for an instant ($t = 597$ s) at which the flashover occurs. The maximum value of the soot layer thickness at which the flashover occurs is about $20 \mu\text{m}$.

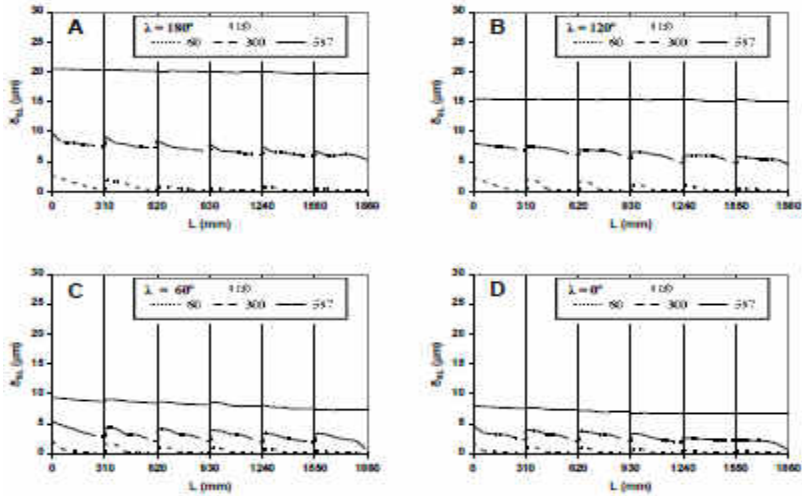


Fig. 5 Time evolution of the deposited soot layer thickness along the leakage path for different locations on the insulator string.

Figure 6 shows the time evolution for the distribution of the deposited soot layer temperature. Same range of temperature rise above the ambient (up to 25 K) has been reported for normally polluted insulators in the literature [39]. A clear variation of the soot layer temperature along the leakage path is observed even at the instant of flashover ($t = 597$ s) where the soot layer thickness is nearly constant. This variation is mainly due to the variation of the tangential component of the electric field strength, $E_{t,L}$ as will be demonstrated in Fig. 12. The value of $E_{t,L}$ is a dominant factor in the thermal energy generation term controlling the rise of the soot layer temperature. Higher values of soot-layer temperature rise (up to 60 K) are expected with fires occurring at lower wind velocities and in hotter ambient.

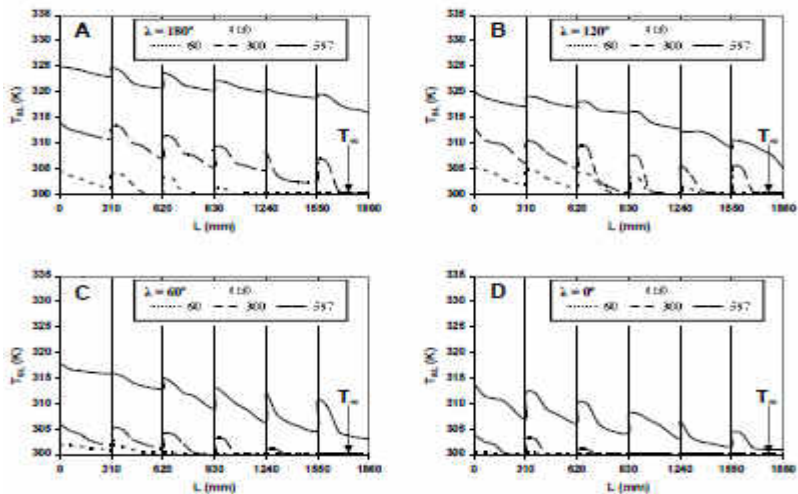


Fig. 6 Time evolution of the deposited soot layer temperature along the leakage path for different locations on the insulator string.

Figure 7 shows the time evolution for the distribution of the deposited soot-layer surface resistance. The figure indicates that the average values of the soot layer resistance (10 - 100 Ω) are much smaller than those values presented in published works ($10^4 - 10^{11}$ Ω) for normally polluted insulators [40]. This is mainly due to the high value of the electric conductivity for the soot material (1500 S/m at 300 K) compared with insulator polluting materials used by other researchers having the order of 10 - 50 $\mu\text{S/m}$. The nearly constant value of the soot-layer surface resistance along the leakage path at the time of flashover is mainly due to the nearly constant value of the soot layer thickness. The effect of the variation in the electric conductivity of the soot layer caused by the temperature rise is negligible due to small values of temperature rise shown in Fig. 6. Accordingly, the variation of the soot-layer surface resistance over the different leakage paths can be understood in the view of the variation of the soot layer thickness as shown in Fig. 5.

Figure 8 shows the effect of varying the system voltage on the deposition of the soot layer at the beginning point of leakage path length ($L = 0$) on the front location ($\lambda = 180^\circ$). The indicated values of the system voltage represent the common rated values for transmission system voltages. The rate of soot deposition decreases and consequently, the accumulated soot layer thickness decreases as the system voltage increases. This can be explained as follows. The electric field possesses large strength values with higher system voltages. The source of momentum (Eq. 3) in the present model accelerates most of the soot particles incident to the insulator surface resulting in less deposition rate. The figure shows that flashover occurs earlier with small soot layer thicknesses associated with higher system voltages. This is due to mainly the significant increase in the tangential component of the electric field strength and by turn, the leakage current increase. The results for lower system voltage of 10 kV show no flashover occurrence up to an assigned time of 600 s (duration of fire propagation).

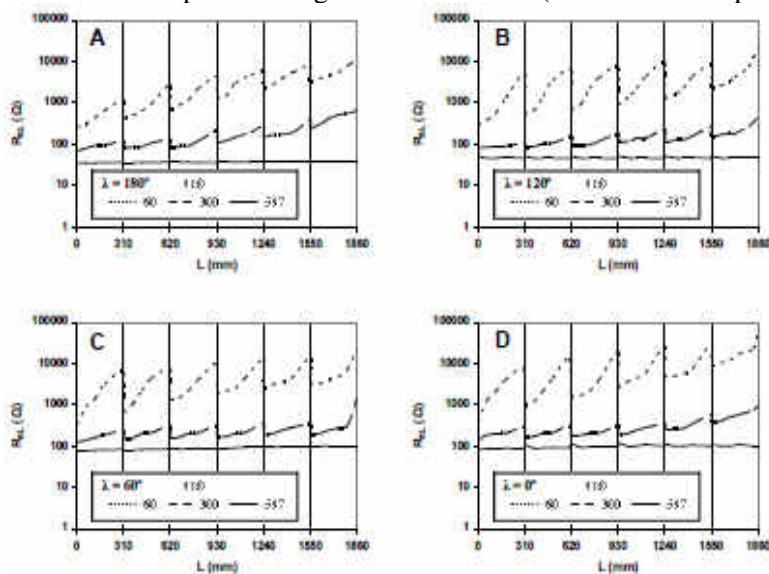


Fig. 7 Time evolution for the surface resistance of the deposited soot layer along the leakage path for different locations on the insulator string.

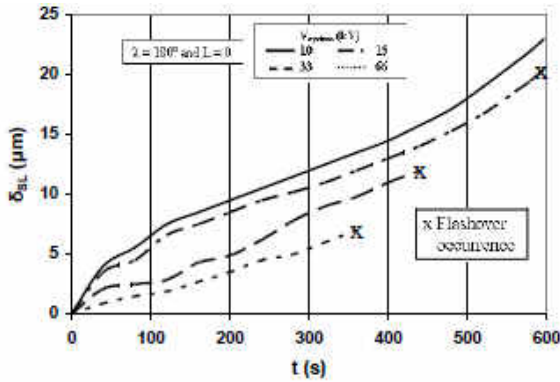


Fig. 8 Effect of varying the system voltage on the deposition of the soot layer.

3.2 Electric Field Distribution over the Insulator Surface

Figures 9 and 10 show the results for the distribution and time evolution of the potential and the electric field strength over the insulator surface, respectively. The initial distributions shown ($t = 0$) are typical for purely capacitive electric field over clean insulators commonly used with high voltage transmission lines. The distributions change with time from purely capacitive to capacitive-resistive as the surface resistance decreases gradually with the accumulation of the deposited soot layer (Fig. 7). The electric field becomes almost resistive along the leakage path when and where the flashover occurs ($t = 597$ s and $\lambda = 180^\circ$). The features shown in Figs. 9 and 10 of the resistive electric field are understood from the nearly linear distribution of the potential and the nearly constant value of the electric field strength along the leakage path. Similar results for artificially polluted insulators have been reported [39,40].

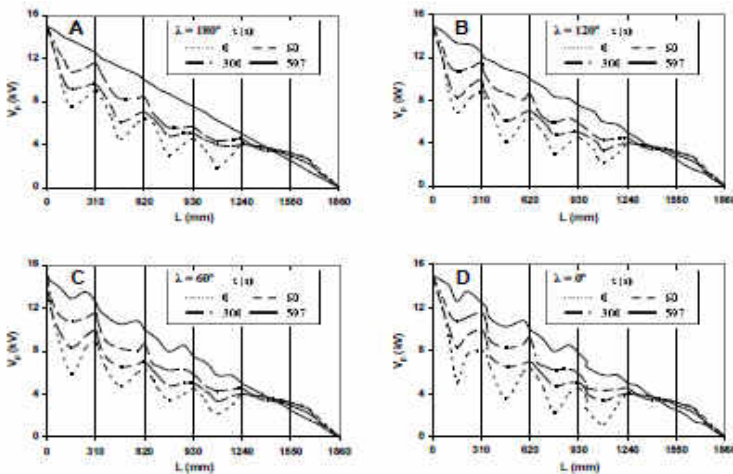


Fig. 9 Time evolution for potential along the leakage path for different locations on the insulator string.

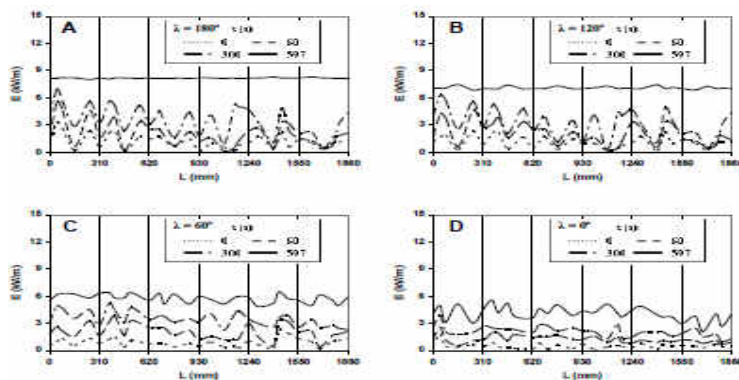


Fig. 10 Time evolution for electric field strength along the leakage path for different locations on the insulator string.

3.3 Characteristics for Flashover Occurrence

Figure 11 shows small fluctuations in the calculated local leakage current along the leakage path at different time instants. These fluctuations probably are due to numerical errors in calculating the local values of the leakage current. Therefore, it was reasonable to consider the accurate value of the leakage current as the average of its local values (Eq. 19). The figure also shows that the leakage current increases with time till a limiting value of 2.15 A at which flashover occurs. Same range of leakage current values for flashover occurrence (0.5 - 3 A) has been reported even with normally polluted insulators with pollutant resistance as high as 0.014 - 2 M Ω [41]. For those insulators, large electric field strengths are expected to exist with the associated large system voltages and small leakage path lengths. The resulting large values of the electric field strength combined with the large normal pollutant resistances nearly generate a situation similar to the present severely polluting case of fire-produced soot (< 34 Ω).

Figure 12 shows the time evolution for the distribution of the tangential component of the electric field strength $E_{t,L}$ and the associated values of the arc electric field strength E_{arc} . The earlier distributions of the tangential component of the electric field strength $E_{t,L}$ exhibit significant non-uniformity with maxima and minima. Then with time, the distributions become nearly uniform with increasing values. The value of E_{arc} decreases with time till it is exceeded by the value of $E_{t,L}$ along 67% of the total leakage path length at the front location ($\lambda = 180^\circ$), causing the flashover to occur. This condition is not satisfied at other locations where partial arcs occur without flashover ($\lambda = 120^\circ$ and 60°) or partial arcs do not occur at rear locations ($\lambda = 0^\circ$). The numerical values of the tangential component of the electric field strength $E_{t,L}$ are comparable with the values reported before [39,40].

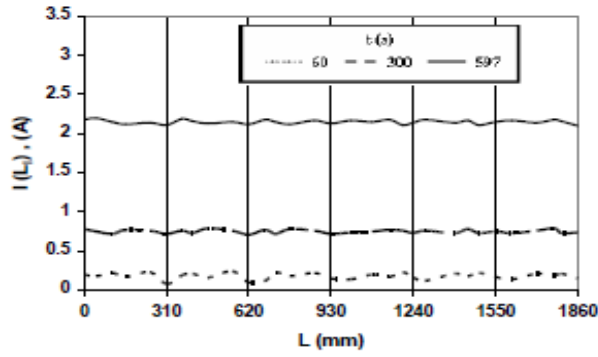


Fig. 11 Time evolution for the variation of the leakage current along the leakage path.

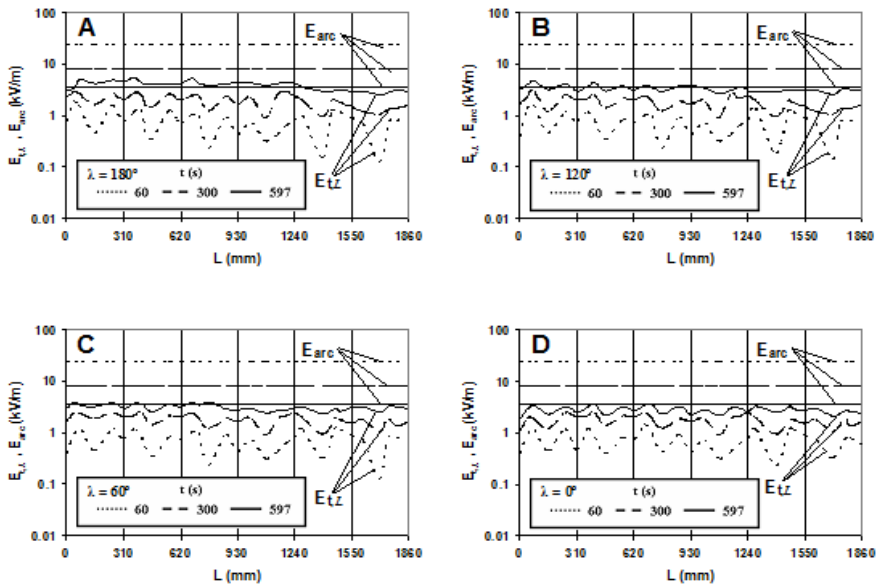


Fig. 12 Time evolution for tangential and arc electric field strength along the leakage path for different locations on the insulator string.

4. CONCLUSIONS AND FUTURE WORK

The present study formulates and solves a non-steady three-dimensional mathematical integrated model for flashover due to the deposition of fire-produced soot particles on high voltage insulators. The model accurately simulates the simultaneous real events involved in the multi-phase flow of fire products as well as the mechanism of soot deposition leading to the flashover. Model numerical predictions for a representative case study were presented and discussed to check the model validity and accuracy. According to the discussion of the results for the selected case study, the validity of the present model is ensured through its physically acceptable predictions. The general agreement of the present model predictions with the limited results available in the literature adds more evidence for the model validity. The discussion also, emphasizes the ability of the present model to describe in detail the temporal and spatial variations of all flow properties which are necessary to be treated. These features confirm the

present model accuracy in predicting the flashover characteristics for the severe case of soot pollution. The model forms a satisfactory tool in designing and dimensioning the insulators of high voltage transmission lines to avoid their expected fire-caused outages. The predictions of the present model can be extended to cover wide range of real cases other than the present selected case. Such cases are associated with different conditions including orientation and configuration of the burnt field, shape and dimensions of the insulator string, and the existence of fire-produced solid particles other than soot. More wide application of the present model can be achieved with the addition of appropriate sub-models accounting for the general parameters affecting the mechanism of solid particles deposition on insulator surfaces. These parameters include particle shape and size distribution, accurate expression for the particle capture velocity, and insulator surface roughness.

REFERENCES

- [1] A. Robledo-Martinez, E. Guzman, and J. L. Hernandez, "Dielectric characteristics of a model transmission line in the presence of fire", *IEEE Trans Electr Insul*, 26(4), 1991, pp. 776-782.
- [2] G. L. W. Perry, "Current approaches to modeling the spread of wildland fire: a review", *Prog. Phys. Geogr.*, 22(2), 1998, pp.222-245.
- [3] D. Morvan and J. L. Dupuy, "Modeling of fire spread through a forest fuel bed using a multiphase formulation", *Combust Flame*, 127, 2001, pp. 1981-1994.
- [4] D. Morvan and J. L. Dupuy, "Modeling the propagation of a wildfire through a Mediterranean shrub using a multiphase formulation", *Combust. Flame*, 138, 2004, pp. 199-210.
- [5] B. Porterie, J. L. Consalvi, J. C. Loraud, F. Giroud, and C. Picard, "Dynamics of wildland fires and their impact on structures", *Combust Flame*, 149, 2007, pp. 314-328.
- [6] N. Sardoy, J. L. Consalvi, B. Porterie, and A. C. Fernandez-Pello, "Modeling transport and combustion of firebrands from burning trees", *Combust Flame*, 150, 2007, pp. 151-169.
- [7] E. H. El-Zohri, H. M. Shafey, M. Abdel-Salam, and A. Ahmed, "Mathematical modeling of agricultural fires beneath high voltage transmission lines", *Energy*, 36, 2011, pp. 385-396.
- [8] G. N. Bae, C. S. Lee, and S. O. Park, "Measurements and control of particle deposition velocity on a horizontal wafer with thermophoretic effect", *Aerosol Science and Technology*, 23(3), 1995, pp. 321-330.
- [9] A. Petroff and L. Zhang, "Development and validation of a size-resolved particle dry deposition scheme for application in aerosol transport models", *Geosci. Model Dev.*, 3, 2010, pp. 753-769.
- [10] A. Guha, "Transport and deposition of particles in turbulent and laminar flow", *Annu. Rev. Fluid Mech.*, 40, 2008, pp. 311-341.
- [11] J. Y. Tu, J. H. Yeoh, Y. S. Moris, and W. Yang, "A study of particle rebounding characteristics of a gas-particle flow over a curved wall surface", *Aerosol Science and Technology*, 38, 2004, pp. 739-755.

- [12] Y. S. Morsi, J. Y. Tu, J. H. Yeoh, and W. Yang, "Principal characteristics of turbulent gas-particulate flow in the vicinity of single tube and tube bundle structure", *Chemical Engineering Science*, 59, 2004, pp. 3141-3157.
- [13] Z. F. Tian, "Numerical modeling of turbulent gas-particle flow and its applications", Ph D Thesis, School of Aerospace, Manufacturing & Mechanical Engineering, RMIT University, Australia, 2006.
- [14] Z. Zhang and Q. Chen, "Prediction of particle deposition onto indoor surfaces by CFD with a modified Lagrangian method", *Atmospheric Environment*, 43(2), 2009, pp. 319-328.
- [15] J. R. Valentine and P. J. Smith, "Numerical predictions of deposition with a particle cloud tracking technique", Report, Department of Chemical and Fuels Engineering, University of Utah, Salt Lake City, UT, USA, 1998.
- [16] B. D. Cohan, "Verification and validation of the soot deposition model in fire dynamics simulator", M Sc Thesis, Faculty of Graduate School, University of Maryland, College Park, USA, 2010.
- [17] A. Coppalle, P. E. Damay, D. Maro, M. Talbaut, O. Connan, and D. Hébert, "Validation of aerosols dry deposition velocity models with new data", 13th Conference on Harmonisation within Atmospheric Dispersion Modeling for Regulatory Purposes, Paris, France, 2010, pp. 658-661.
- [18] G. Shrestha, S. J. Traina, and C. W. Swanson, "Black carbon's properties and role in the environment: a comprehensive review", *Sustainability*, 2, 2010, pp. 294-320.
- [19] L. L. Alston and S. Zoledziowski, "Growth of discharges on polluted insulators", *Proc. IEE*, 110, 1963, pp. 1260-1266.
- [20] B. F. Hampton, "Flashover mechanism of polluted insulation", *Proc. IEE*, 111, 1964, pp. 985-900.
- [21] H. Boheme and F. Obenaus, "Pollution flashover tests on insulators in the laboratory and in systems and the model concept of creepage path flashover", *Cigré*, 1966, paper 407.
- [22] R. Wilkins, "Flashover voltage of high voltage insulators with uniform surface pollution films", *Proc. IEE*, 116, 1969, pp. 457-465.
- [23] F. A. M. Rizk, "Mathematical models for pollution flashover", *Electra*, 78, 1981, pp. 71-103.
- [24] R. Sundararajan and R. S. Gorur, "Dynamic arc modeling of pollution flashover of insulators under dc voltage", *IEEE Trans. Electr. Insul.*, 28, 1993, pp. 209-218.
- [25] R. Sundararajan, N. R. Sathureddy, and R. S. Gorur, "Computer-aided design of porcelain insulators under polluted conditions", *IEEE Trans. Dielectrics Electr. Insul.*, 2, 1995, pp. 121-127.
- [26] N. Dhahbi-Megrache and A. Beroual, "Flashover dynamic model of polluted insulators under ac voltage", *IEEE Trans. Dielectrics Electr. Insul.*, 7, 2000, pp. 283-289.
- [27] R. Boudissa, S. Djafri, A. Haddad, R. Belaicha, and R. Bearsch, "Effect of insulator shape on surface discharges and flashover under polluted conditions", *IEEE Trans. Dielectrics Electr. Insul.*, 12, 2005, pp. 429-437.
- [28] M. T. Gencoglu and M. Cebeci, "Computation of AC flashover voltage of polluted HV insulators using a dynamic arc model. Euro", *Trans. Electr. Power*, 10, 2008, pp. 249-262.

- [29] T. C. Chen and H. I. M. Nour, "A study on the profile of HVDC insulators", *IEEE Trans. Electr. Insul.*, 24, 1989, pp. 113-117.
- [30] T. C. Chen, H. I. M. Nour, and C. Y. Wu, "DC interfacial breakdown on contaminated electrolytic surfaces", *IEEE Trans. Electr. Insul.*, 19, 1984, pp. 536-542.
- [31] H. A. M. Al-Nehari, "A study on the effects of air pollutants and dispersion in urban atmospheres", Ph D Thesis, Department of Mechanical Engineering, Faculty of Engineering, Assiut University, Assiut, Egypt, 2010.
- [32] F. P. Incropera and D. P. Dewitt, "Introduction to Heat Transfer", Wiley, NY, third ed., 1992.
- [33] H. Singer, H. Steinbigler, and P. Weiss, "A charge simulation method for the calculation of high voltage fields", *IEEE Trans. on PAS*, 93, 1974, pp. 1660-1668.
- [34] T. Takuma and T. Kawamoto, "Field calculation including surface resistance by charge simulation method", 3rd Int. Symp. on HV Eng., Milan, Italy 1979, paper no. 12-01.
- [35] T. Takuma, T. Kawamoto, and H. Fujinami, "Charge simulation method with complex fictitious charges for calculating capacitive-resistive fields", *IEEE Trans. on PAS*, 100, 1981, pp. 4665-4672.
- [36] F. Gutfleisch, "Berechnung elektrischer Felder durch Nachbildung der Grenzschichten mit ausgewählten Flächenelementen", Diss. Technischen Universität Hamburg-Harburg, 1989.
- [37] G. G. Karady and F. Amrah, "Dynamic modeling of AC insulator flashover characteristics", *IEE Symposium on High Voltage Engineering*, No. 467, August 1999, pp. 107-110.
- [38] S. V. Patankar, "Numerical Heat Transfer and Fluid Flow", Hemisphere Publishing Corporation, NY, 1980.
- [39] G. Xu and P. B. McGrath, "Electrical and thermal analysis of polymer insulator under contaminated surface conditions", *IEEE Trans. Dielectrics Electr. Insul.*, 3(2), 1996, pp. 289-298.
- [40] S. Chakravorti and P. K. Mukherjee, "Power frequency and impulse field calculation around a HV insulator with uniform or nonuniform surface pollution", *IEEE Trans. Electr. Insul.*, 28(1), 1993, pp. 43-53.
- [41] E. M. M. El-Refai, M. T. El-Noaman, and M. K. Mohamed, "Dynamic arc modeling of pollution flashover process on HV insulators under AC voltage", 13th Middle East Power Systems Conference, MEPCON'2009, Assiut University, Egypt, 2009, pp. 662-667.

النمذجة الرياضية للقوس الومضى الناشئ من ترسب حبيبات سناج الحريق على عوازل التعليق لخط نقل عالي الجهد

في كثير من الأحيان ينشب حريق في الحقول الزراعية التي تمر عبرها خطوط النقل عالية الجهد وينتج عنه ترسب سناج الحريق على عوازل هذه الخطوط. هذا السناج بدوره يؤدي إلى حدوث مشكلة القوس الومضى الذي يتسبب في انقطاع التغذية لهذه الخطوط ممثلاً بذلك خسائر اقتصادية كبيرة لكل من الشبكة الكهربائية ومستخدميها. هذه المشكلة مهمة وتمثل مجموعة من الظواهر الطبيعية والعمليات الكيميائية المعقدة التي تحتاج فهماً متعمقاً لوصفها ونمذجة المعادلات والعلاقات الرياضية الحاكمة لها. يعرض هذا البحث نموذجاً رياضياً متكاملًا يحاكي الأحداث المتزامنة التي تؤدي لوقوع القوس الومضى. يتضمن النموذج تحليلاً للانسياب ثلاثي الأبعاد لنواتج الحريق متعددة الطور في الحالة غير المستقرة. هذا ويصف النموذج بالتفصيل آلية ترسب السناج الناتج فوق أسطح العوازل بشكل مترافق مع عملية نشوء وتغير المجال الكهربى حولها. تحل المعادلات الآتية للنموذج بطريقة عددية تكرارية تستخدم الحجم المحدودة مع العناصر الجدارية غير المباشرة وطريقة محاكاة الشحنة لحساب الجهد الكهربى. يعرض البحث مناقشة النتائج العددية لدراسة حالة تخص سلسلة عوازل لخط نقل بجهد 15 كيلوفولت. تتضمن هذه المناقشة مقارنة النتائج لخصائص طبقة السناج المترسبة وتوزيع الجهد الكهربى وخصائص حدوث القوس الومضى مع النتائج المتاحة فى المراجع المنشورة. وقد أثبتت المناقشة والمقارنة صحة ودقة النموذج المعروف فى هذا البحث.